PHYSICAL REVIEW B **101**, 085414 (2020)

Evaluation of surface roughness of metal films using plasmonic Fano resonance in attenuated total reflection

Munehiro Nishida,[1,*] Taisei Matsumoto,[1] Hiroya Koga,[1] Terukazu Kosako,[2] and Yutaka Kadoya[1]
[1]*Graduate School of Advanced Science of Matter, Hiroshima University, Higashi-Hiroshima, 739-8530, Japan*
[2]*YAZAKI Research and Technology Center, 1500 Mishuku, Susono-city, Shizuoka, 410-1194, Japan*

(Received 15 September 2019; revised manuscript received 3 January 2020; accepted 29 January 2020; published 20 February 2020)

Attenuated total reflection (ATR) by surface plasmon polariton (SPP) is a method for evaluating the dispersion relation of SPP from the position of a dip in the reflection spectrum. However, recent studies have shown that the dips are displaced from SPP resonance because they are produced by a type of Fano resonance, i.e., the interference between the resonant reflection process accompanied by resonant excitation of SPP and the direct reflection process without resonant excitation. This result suggests that the system properties difficult to be achieved in the dispersion relation of SPP can be characterized using the ATR method. In this study, we investigate the effect of surface roughness due to nanosized dimples created in the initial stage of pitting corrosion on the ATR spectrum, from the viewpoint of Fano resonance. Using the temporal coupled-mode method, it is shown that the Fano resonance in ATR is caused by the phase change of direct reflection because of the absorption on the metal surface, and the spectral shape is determined by this phase, along with the ratio of the external (radiative) decay rate to the total decay rate of the resonant mode. Moreover, it is clarified that the internal and external decay rates extracted from the ATR spectrum provide information on corrosion, such as the effective thickness of the metal film and the randomness in dimple distribution.

DOI: 10.1103/PhysRevB.101.085414

I. INTRODUCTION

Surface plasmon resonance sensors using resonant absorption by surface plasmon polariton (SPP) are practically realized as highly sensitive, refractive index sensors, and used widely in the fields of chemistry and biotechnology [1–3]. Kretschmann configuration is the most popular structure of a surface plasmon resonance sensor, which uses the attenuated total reflection (ATR) caused by SPP on a thin metallic film evaporated on a prism [4]. ATR is a phenomenon that produces sharp dips in the reflection spectra at a specific incident angle or incident wavelength due to the resonant excitation of SPP through the evanescent wave produced by the total reflection of the prism.

It is considered that the dips in ATR originate from the material loss of the metal film during the resonant excitation of SPP, and that the dip position directly corresponds to the dispersion relation of SPP. Kretschmann derived a Lorentzian spectral function typical for resonant phenomena by approximating an exact reflection coefficient for a three-layer structure near the resonant wave number of SPP [5,6]. This result is the basis of the above view and was used in interpreting the results of subsequent studies. In this view, the change in the dispersion relation of SPP (relation between the incident angle and resonant frequency) appears directly in the position change of the dip, and enables to evaluate the change in the refractive index of the ambient medium using the expression of the dispersion relation.

However, recent studies [7,8] have shown that resonant dips are produced by a type of Fano resonance [9]. There appears a shift between the complex wave numbers of the reflection coefficient pole (complex resonant wave number) and the reflection coefficient zero (complex zero-point wave number) due to the metallic loss. As a result, there appears an asymmetric peak-dip structure in the spectrum. Such behavior of the reflection coefficient can be interpreted as a result of the interference between the resonant reflection process accompanied by the excitation of the resonant mode and the direct reflection process without resonant excitation.

There is a shift between the dip and resonant positions in the Fano spectrum, whose size is determined by the interference of the two reflection processes and changes in a complicated manner with a change in the amplitude and phase of the reflected waves. Therefore, calibration using the measured value of the real system is necessary to precisely evaluate the refractive index of the ambient medium. On the other hand, using the notion of Fano resonance, the properties that are difficult to be achieved in the dispersion relation of SPP (the real part of the complex resonant frequency) can be evaluated. For example, diffusive scattering caused by the surface roughness affects the interference between resonantly reflected wave and directly reflected wave, and may shift the position of the dip (peak) produced by destructive (constructive) interference.

Indeed, there have long been studies evaluating the roughness of a metal surface using the ATR method [6,10]. Experimental studies have shown that the effects of surface roughness are clearly seen as changes in dip position and width [10–15]. In addition, there have been attempts to study

---

[*] mnishida@hiroshima-u.ac.jp

the corrosion resistance of the metal by observing these changes in the ATR method [16,17]. However, theoretical studies that treated the effect of roughness as perturbation have shown that second-order approximation is necessary for describing the influence of roughness on the SPP dispersion relation, which gives about a factor 10 smaller change in the dip position as compared to the observed data [6,18]. Although attempts have been made to explain the difference between theory and experiment in a specific situation [19], as far as we know, there is no theory that can quantitatively estimate the effect of roughness of a metal surface on the dip position in general systems. What is lacking here is the viewpoint that the dip and the dispersion relation of SPP are not directly related but displaced with each other due to Fano resonance. From this viewpoint, the results of experiments and theories obtained so far are consistent.

Thus, reconsideration of the ATR method from the viewpoint of Fano resonance will provide information on the system property, e.g., the progress of corrosion, with high accuracy. Especially, at the initial stage of pitting corrosion [20–22], nanosized pits are created on the metal surface and can cause strong diffusive scattering to SPP. This is expected to influence the shape of the reflection spectrum via Fano resonance, and may enable the deduction of the initial progress of pitting corrosion from the spectral shape. Pitting is a type of localized corrosion that occurs in a metal with a passivation film, such as aluminum alloy or stainless steel. It is a dangerous process, causing accelerated localized dissociation of metals that trigger mechanical failures or stress corrosion cracking. Therefore, it is quite important to detect its initial process. If the roughness of the metal surface can be read accurately from the ATR spectrum, it will become possible to detect the initial process of pitting corrosion on nanoscale.

In this paper, to build a base to quantitatively deduce the roughness of metal surfaces from a spectral shape, the relation between the ATR spectrum and metal surface condition is clarified by analyzing the Fano resonance in the ATR of Kretschmann configuration using the temporal coupled-mode (TCM) method [23–25] and the spatial coupled-mode (SCM) method [25–27]. Especially, distribution of cylindrical dimples is used for a model of surface roughness or pits created in pitting corrosion. The effect of the periodic and random arrays of dimples on the ATR spectrum is studied in detail. Specifically, first, we identify the parameters that determine the shape of the resonant spectrum based on the expression of the reflection coefficient obtained using the TCM method. Next, we calculate the reflection spectrum by using the SCM method and extract parameters for a system composed of a flat metal film with various thicknesses and material loss and for a system composed of an aluminum film with a periodic or random array of cylindrical dimples. Finally, we study the correlation between the parameters and the condition of the metal film to verify the possibility of evaluating the pitting corrosion from the ATR spectrum shape.

System

Figure 1 shows a schematic of our concerned system. Cylindrical dimples are created periodically or randomly in the aluminum thin film evaporated on a SiO_2 substrate. To account for the natural oxide film created on the surface of the aluminum film, a homogeneous Al_2O_3 film with a thickness of 2.7 nm covers the aluminum film even at the top of the dimple. Although it is plausible that the oxide film at the top of the dimple is removed, we omit this effect because it produces only a small change in the reflection spectrum.

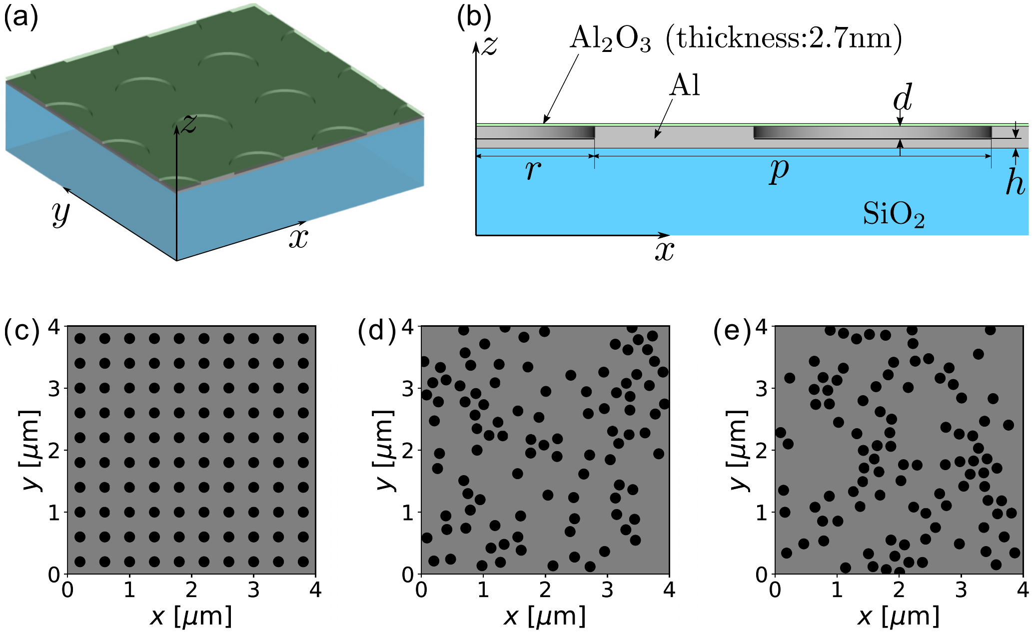

FIG. 1. System configuration. (a) Schematic of a cylindrical nanodimple array created on an aluminum film. (b) A cross section of the system. (c) Configuration of a periodic dimple array. (d), (e) Random arrangements of dimples that produce the smallest (d) and largest (e) internal losses in 100 samples.

In what follows, it is assumed that the radius and depth of the cylindrical dimple are r and d, respectively; the thickness of the aluminum film left below the bottom of the dimple is h; and the period of the periodic dimple array is p, as shown in Fig. 1(b). The refractive indices of the SiO_2 substrate and Al_2O_3 film are 1.457 and 1.6764, respectively, and the space above the Al_2O_3 film and the inner space of the dimples are filled with a NaCl solution whose refractive index is 1.338. The Drude-Lorentz model, proposed in [28], is used for the dielectric function of aluminum $\varepsilon_{\mathrm{Al}}(\omega)$.

We focus on the resonant structure that appears in the incident-angle dependence of zeroth-order reflection when an incident light with wavelength $\lambda_{\mathrm{i}} = 650$ nm is irradiated from the substrate side under the total reflection condition. We study the spectral change in the following three cases to reveal the influence of the surface condition on the spectral shape: Without dimples ($d = 0$ nm, corresponding to a flat metal film), with a periodic dimple array [Fig. 1(c)], and with a random dimple array [Figs. 1(d) and 1(e)]. Here, the random array is composed of randomly placed cylindrical dimples with a radius of 80 nm. We produce 100 samples of a random dimple array under the condition that the distance between adjacent dimples is not less than 60 nm and 100 dimples exist in the 4 μm × 4 μm area, which is the calculation area imposed by the periodic boundary condition along the x and y directions. We select three samples from the 100 samples in which the effect of diffusive scattering is considered minimum [Fig. 1(d)], maximum [Fig. 1(e)], and near the average, judging from the analysis of the spectral shape factor described below. In what follows, we will present only the data of these three samples for random arrays.

II. METHODS

A. Temporal coupled-mode method

Kretschmann configuration in plasmonic ATR is a system in which a cavity with a single resonant mode corresponding to SPP is attached to a single input/output port representing a connection with the incident and reflected waves. The TCM method describes resonant scattering phenomena in a unified way by considering the dynamics of cavities attached to ports [23–25]. Therefore, our system can be described by the TCM method, which reproduces general features of the resonant spectrum by setting a few parameters, and is effective in understanding the origin of the resonance.

In the case where the cavity couples with the port weakly, the amplitude of the resonant mode with a resonant angular frequency of ω_{r} is described by the following coupled-mode equation [23,24,29]:

$$\begin{aligned}\frac{da}{dt} &= -i\omega_{\mathrm{r}}a - \gamma a + \kappa s_+,\\ s_- &= r_{\mathrm{d}}e^{i\phi_{\mathrm{d}}}s_+ + da,\\ \gamma &= \gamma_{\mathrm{i}} + \gamma_{\mathrm{e}}.\end{aligned} \tag{1}$$

Here, γ_{i} denotes the internal decay rate due to the loss of the materials composing the cavity and γ_{e} denotes the external decay rate due to the loss caused by the radiation to the port. The variables s_+ and s_- denote the amplitudes incoming and outgoing the radiative modes through the port, respectively, where the mode fields are normalized so that $|s_\pm|^2$ denote the powers of the modes. The parameters r_{d} and ϕ_{d} denote the magnitude and phase of the direct reflection coefficient, which determines the reflection process in which the incoming wave from the port is reflected directly to the port without the resonant excitation. The parameter κ (d) denotes the coupling constant between the incoming (outgoing) mode and cavity mode through the port.

In the case where the internal loss of the resonant mode, the energy absorption in the direct reflection process, and the coupling to the port are all weak, the parameters γ_{e}, d, and κ can be approximately treated as independent of the internal decay rate γ_{i} and absorption in the direct reflection process. Considering the case where $\gamma_{\mathrm{i}} = 0$ and the direct reflection coefficient is expressed as $r_{\mathrm{c}} = e^{i\phi_{\mathrm{c}}}$, the relations $|d|^2 = 2\gamma_{\mathrm{e}}$, $r_{\mathrm{c}}d^* = -d$, and $d = \kappa$ are obtained from the principle of conservation of energy and the time-reversal symmetry [24]. For continuous-wave incidence with the angular frequency of ω, the reflection coefficient is expressed as (see Supplemental Material [30] for the derivation)

$$\begin{aligned} r(\omega) &= r_{\mathrm{d}}e^{i\phi_{\mathrm{d}}}\left(1 - \frac{2i\frac{\gamma_{\mathrm{e}}}{r_{\mathrm{d}}}e^{i\phi}}{\omega - \omega_{\mathrm{r}} + i\gamma}\right)\\ &= r_{\mathrm{d}}e^{i\phi_{\mathrm{d}}}\left(\frac{\omega - \omega_0 + i\gamma_0}{\omega - \omega_{\mathrm{r}} + i\gamma}\right), \end{aligned} \tag{2}$$

$$\omega_0 = \omega_{\mathrm{r}} - 2\sin\phi\gamma_{\mathrm{e}}/r_{\mathrm{d}},\ \ \gamma_0 = \gamma - 2\cos\phi\gamma_{\mathrm{e}}/r_{\mathrm{d}}. \tag{3}$$

Thus, the change in the phase of direct reflection due to absorption $\phi = \phi_{\mathrm{c}} - \phi_{\mathrm{d}}$ makes the shape of the reflection spectrum asymmetric and shifts the minimum from the resonance condition.

B. Spatial coupled-mode method

The SCM method describes the electromagnetic field in the metal film with nanoholes by waveguide modes in the nanohole. It enables a semiquantitative calculation for reflectance and transmittance with a small computational resource and high speed. However, because it is assumed that the electromagnetic field becomes zero inside the metal film in the SCM method developed so far, it is not possible to accurately describe a system with a thin metal film in which the effect of tunneling through the film is large. To make the SCM method applicable to the system with a thin metal film, we make the following improvements (see Supplemental Material [30] and Refs. [31–36] therein for the derivation):

(i) to adopt the boundary condition considering the penetration of electromagnetic wave inside the metal (transition boundary condition [37] with in-plane wave-number dependence);

(ii) not to use mean-field approximation for the inner product of the waveguide mode and plane wave [27];

(iii) to fix reciprocity using the scattering matrix.

As mentioned in the last item, we use a scattering matrix that enables to calculate spectra for arbitrary multilayer films by using recurrence formula [38]. Therefore, the usual Kretschmann configuration without the layer of nanohole array can be treated similarly.

Through the above treatments, the quantitativity of the SCM method for a system that contains a metallic thin film is improved enough to yield almost the same result as that obtained using the rigorous coupled-wave analysis (RCWA) method [38] as shown in Fig. S2 in the Supplemental Material [30].

III. RESULTS AND DISCUSSION

A. Fano resonance spectral profile in attenuated total reflection

Consider the case where the angular spectra near the resonant angle are obtained using a focused incident light with an angular frequency of $\omega_{\mathrm{i}} = \frac{2\pi}{c\lambda_{\mathrm{i}}}$, where c is the speed of light in vacuum. The wave-number dependence of resonant angular frequency in the narrow range near ω_{i} can be approximated as linear, and other parameters as constants. In this case, the concrete formula of wave-number dependence of the reflectance can be obtained from the formula of the TCM method (2).

First, we assume that the resonant wavelength at which SPP is resonantly excited by the incident light with the angular frequency of ω_{i} is denoted by k_{r}, in other words, the dispersion relation of SPP passes through the point $(k_{\mathrm{r}}, \omega_{\mathrm{i}})$. We also assume that the relation between ω_{r} and k_x is linear with the gradient of the group velocity v_{SPP} of SPP on the surface of the semi-infinite metal. Then, the k_x dependence of ω_{r}, namely, the dispersion relation of the resonant mode, is expressed as

$$\omega_{\mathrm{r}} = v_{\mathrm{SPP}}(k_x - k_{\mathrm{r}}) + \omega_{\mathrm{i}}. \tag{4}$$

Taking the values at $k_x = k_{\mathrm{r}}$ for the parameters γ_{e}, γ, r_{d}, and ϕ in Eq. (2), the reflectance $R = |r|^2$ becomes

$$\frac{R(k_x)}{R_{\mathrm{d}}} = \frac{\left\{\frac{v_{\mathrm{SPP}}}{\gamma}(k_x - k_{\mathrm{r}}) - 2\chi\ \sin\phi\right\}^2 + (1 - 2\chi\ \cos\phi)^2}{\left\{\left(\frac{v_{\mathrm{SPP}}}{\gamma}\right)(k_x - k_{\mathrm{r}})\right\}^2 + 1}. \tag{5}$$

Thus, the shape of the reflection spectrum as a function of the normalized wave number $\frac{v_{\mathrm{SPP}}}{\gamma}k_x$ is determined using the following two parameters: Ratio of external decay rate to total decay rate modified by the magnitude of the direct reflection coefficient r_{d},

$$\chi = \frac{\gamma_{\mathrm{e}}}{r_{\mathrm{d}}\gamma}, \tag{6}$$

and the phase change ϕ due to the absorption during direct reflection. Here, $R_{\mathrm{d}} = r_{\mathrm{d}}^2$ is the direct reflection rate.

The wave numbers k_+ and k_-, which provide the maximum and minimum of Eq. (5), respectively, are given by the following equations using $p = \pm 1$, which is the sign of $\sin\phi$, namely, $\sin\phi = p|\sin\phi|$:

$$k_\mp = k_{\mathrm{r}} \pm p\frac{\gamma}{v_{\mathrm{SPP}}} f^\mp(\phi, \chi), \tag{7}$$

$$f^\mp(\phi, \chi) = \frac{\sqrt{(\cos\phi - \chi)^2 + \sin^2\phi} \mp (\cos\phi - \chi)}{|\sin\phi|}. \tag{8}$$

The local maximum R_+ and the local minimum R_- of reflectance are given by

$$R_\pm = R_{\mathrm{d}}\left\{1 \pm \frac{2\chi|\sin\phi|}{f^\pm(\phi, \chi)}\right\}. \tag{9}$$

Thus, the total absorption ($|r|^2 = 0$) is realized when

$$\chi = \frac{\gamma_{\mathrm{e}}}{r_{\mathrm{d}}\gamma} = \frac{1}{2\ \cos\phi}, \tag{10}$$

which is a modified critical coupling condition.

At the midpoint between the wave numbers of the reflectance maximum and minimum, $k_{\mathrm{d}} = \frac{k_+ + k_-}{2}$, the reflectance equals the direct reflection rate (see Supplemental Material [30] for the derivation):

$$R(k_{\mathrm{d}}) = R_{\mathrm{d}}. \tag{11}$$

In addition,

$$R_{\mathrm{r}} = R(k_{\mathrm{r}}) = R_- + R_+ - R_{\mathrm{d}} = R_- + \frac{f^-}{f^+}(R_{\mathrm{d}} - R_-). \tag{12}$$

Considering the relation $f^+ f^- = 1$,

$$f^- = \sqrt{\frac{f^-}{f^+}} = \sqrt{\frac{R_{\mathrm{r}} - R_-}{R_{\mathrm{d}} - R_-}}. \tag{13}$$

These characteristics of the reflection spectrum are shown in Fig. 2(a), where $f^\pm$ is an important factor that determines

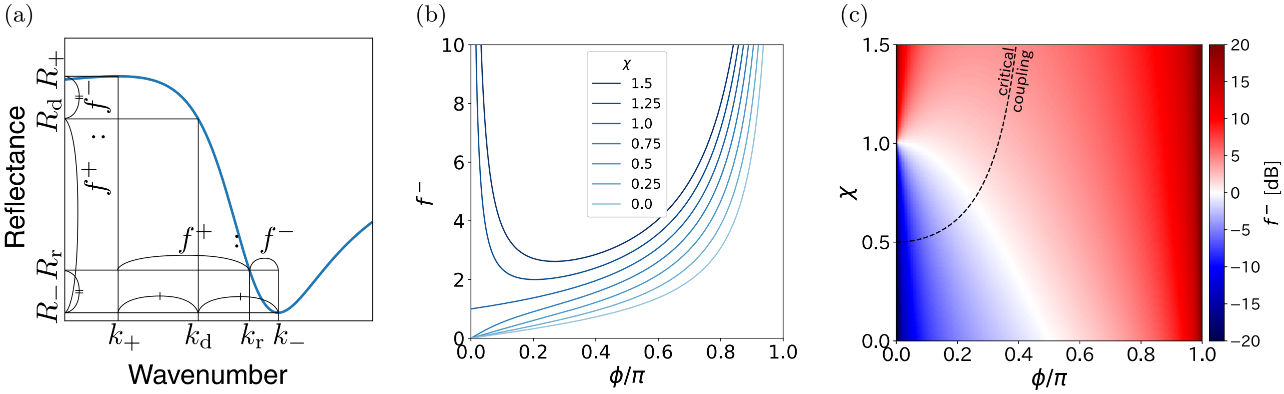

FIG. 2. Characteristics of spectral profile of Fano resonance. (a) Characteristics of the reflection spectrum determined by SSF $f^\pm$. (b), (c) Dependence of SSF on the direct reflection phase ϕ and the ratio of decay rates χ. The dashed line in (c) denotes the critical coupling condition (10).

the spectrum shape. Therefore, we call $f^{\pm}$ the spectral shape factor (SSF) in the following.

Equation (7) shows that the shift of the dip wavelength k_{-} from the resonant wavelength k_{r} is determined by the product of SSF f^{-} and the decay rate γ. Although the shift basically increases with γ, the value of f^{-} can change largely depending on the parameters. Figures 2(b) and 2(c) show the behavior of the change in f^{-} due to the system parameters. We can see that f^{-} can become very large in the case where $\chi > 1$ and $\phi \sim 0$ or in the case of $\phi \sim \pi$. Especially, in the region of a small phase, f^{-} changes discontinuously depending on the value of χ. Therefore, it is important to investigate how parameters χ and ϕ change depending on the system configuration. Because the in-plane wave number k_x is related to the incident angle θ by the relation $k_x = n\frac{\omega_{\mathrm{i}}}{c}\sin\theta$, with n being the refractive index of the prism, it is possible to evaluate the parameters χ, ϕ, γ, and $f^{\pm}$ from the information of the angular spectrum, such as the minimum and maximum points, as shown in the next section.

B. Parameter extraction methods

Because the reflection coefficient $r(\omega)$ can be calculated rapidly by using the SCM method (scattering matrix method for homogeneous multilayer films), we can find the pole $\omega_{\mathrm{r}} - i\gamma$ and the zero $\omega_0 - i\gamma_0$ easily. Then, r_{d} is evaluated as the ratio between $r(\omega)$ and $(\omega - \omega_0 + i\gamma_0)/(\omega - \omega_{\mathrm{r}} + i\gamma)$. From Eq. (3), we obtain

$$\phi = \arctan\left(\frac{\gamma - \gamma_0}{\omega_{\mathrm{r}} - \omega_0}\right), \tag{14}$$

$$\chi = \frac{\gamma_{\mathrm{e}}}{r_{\mathrm{d}}\gamma} = \sqrt{(\omega_{\mathrm{r}} - \omega_0)^2 + (\gamma - \gamma_0)^2}/(2\gamma). \tag{15}$$

In this paper, we call this method parameter extraction by zero-point search (ZPS).

On the other hand, using Eqs. (7), (8), (9), (11), and (13) obtained by the analysis of the TCM method, the values of k_{r}, χ, and ϕ can be deduced from the angle spectrum. The value of R_{d} is obtained from the maximum point (k_{+}, R_{+}) and minimum point (k_{-}, R_{-}) using Eq. (11). Then, f^{-} is determined by reflectance R_{r} at the resonant wavelength k_{r} using Eq. (13). Using Eq. (7), the decay rate can be expressed as $\gamma = v_{\mathrm{SPP}}|k_{-} - k_{\mathrm{r}}|/f^{-}$ and is determined by k_{r}. Using Eq. (9), $\chi\ \sin\phi$ is obtained from R_{d}, f^{-}, and R_{-}, and then using Eq. (8), χ and ϕ can be obtained by considering that γ_0 becomes 0 and $\cos\phi$ changes its sign under the critical coupling condition (10). Therefore, only k_{r} is left for the determination of reflectance of the TCM method (5). In other words, if the value of k_{r} is provided, all parameters included in the reflectance of the TCM method (5) are determined using the SCM spectral data, and the TCM spectral data, such as $R_{\pm}$ and R_{d}, can be obtained. Thus, it is possible to determine the parameters consistently with the model of the TCM method by determining k_{r} so as to minimize the difference between the $R_{\pm}$ and R_{d} values evaluated using the SCM and TCM methods. In this paper, we call this method parameter extraction using the TCM method.

In what follows, after checking the consistence between the two parameter extraction methods, ZPS and TCM, we explore the possibility of characterization of the metal surface condition by studying the variation in SSF depending on the metal surface condition.

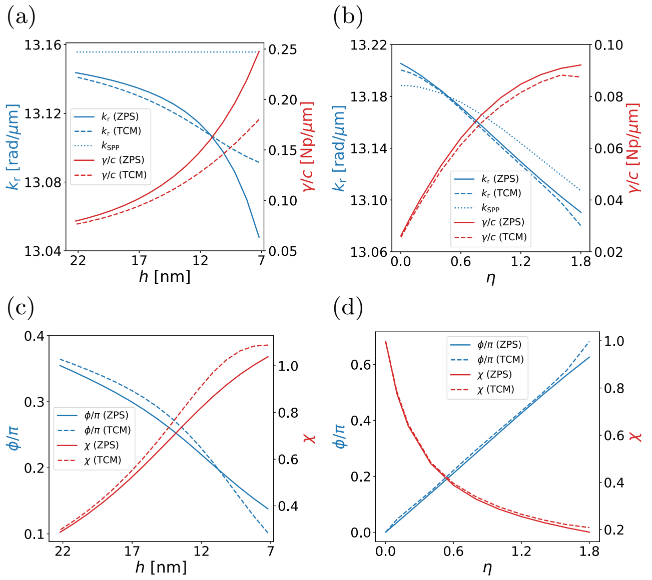

FIG. 3. Extracted parameters for a flat metal film. Solid lines denote the results obtained by parameter extraction by ZPS. Dashed lines denote the results obtained by the parameter extraction by using the TCM method. (a), (b) Wave number k_{r} and decay rate γ of the resonant mode as functions of (a) the metal film thickness h and (b) metal loss factor η. (c), (d) Direct reflection phase ϕ and ratio of decay rates χ as functions of (c) h and (d) η.

C. Flat metal film

First, in a usual Kretschmann configuration without dimples ($d = 0$), we calculate the dependence of the reflection coefficient on the thickness h and the imaginary part of the permittivity of the metal film. Figure 3 compares the parameters extracted using ZPS and those extracted using the TCM method from the reflection coefficient data.

Here, the imaginary part of the permittivity of metal is controlled by the metal loss factor η as $\varepsilon_{\mathrm{m}}(\omega) = \mathrm{Re}[\varepsilon_{\mathrm{Al}}(\omega)] + i\eta\,\mathrm{Im}[\varepsilon_{\mathrm{Al}}(\omega)]$ with $\varepsilon_{\mathrm{Al}}(\omega)$ being the original permittivity of aluminum. In Fig. 3, the resonant wave number k_{r}, the decay rate γ, the change in the direct reflection phase ϕ due to absorption, and the ratio of decay rates $\chi = \frac{\gamma_{\mathrm{e}}}{r_{\mathrm{d}}\gamma}$ are shown as functions of the metal film thickness h and the metal loss factor η. The solid lines depict the parameters extracted by ZPS, while the dashed lines depict the parameters extracted by the TCM method. In Figs. 3(a) and 3(c), we take $\eta = 1$ and change h from 22.2 to 7.2 nm. In Figs. 3(b) and 3(d), we take $h = 22.2$ nm and change η from 0.01 to 1.8. For comparison, the resonant wave number for the SPP on the semi-infinite metal surface is also indicated as a dotted line. These results indicate that appropriate values of parameters can be extracted by the TCM method using only the shape of the angular spectrum in the cases where the metal film thickness h is not less than 10 nm or the metal loss factor η is not more than 1.5. In the case that the thickness of metal film is too thin or the metal loss is too large, the assumptions of weak damping and weak coupling in the derivation of the

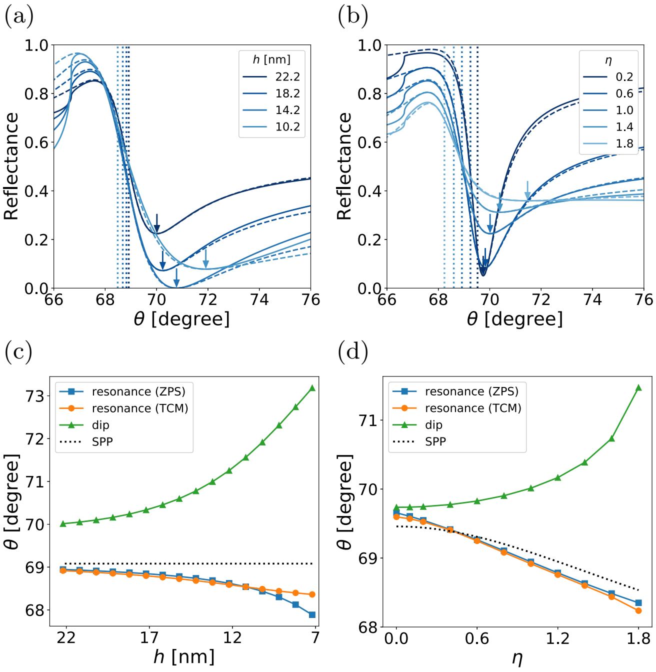

FIG. 4. Resonant and dip angles extracted for a flat metal film. (a), (b) Dependence of angular spectra of reflection on (a) the metal film thickness h and (b) metal loss factor η. Dotted lines depict the resonant angles extracted by the TCM method. Arrows denote the dip positions. (c), (d) Resonant angle extracted by ZPS (blue squares) and by the TCM method (orange circles) and dip angle (green triangles) as functions of (c) h and (d) η. Dotted line depicts the resonant angle obtained using the dispersion relation of SPP.

TCM method are violated and the approximation of the TCM method becomes worse (see Supplemental Material [30] for the derivation of the TCM method).

Figure 4 shows the angular spectra of reflection, the dip angle, and the resonant angle. Figure 4(a) shows the change in the spectrum as the metal film thickness h changes from 22.2 to 10.2 nm. The solid lines depict the results obtained by the SCM method, and the dashed lines depict the results obtained from Eq. (5) using the parameters extracted by the TCM method. We can see that the spectrum obtained by the TCM method reproduces well the behavior around resonance. Figure 4(b) shows the angular spectra of reflection calculated in the cases where the imaginary part of the metal permittivity is multiplied by the metal loss factor η from 0.2 to 1.8. This result also indicates the consistency between the SCM results (solid lines) and TCM results (dashed lines). In Figs. 4(a) and 4(b), the resonant angles extracted by the TCM method are depicted by dotted lines, and the dip positions are depicted by arrows. The changes in these values are summarized in Figs. 4(c) and 4(d), which indicate that both the changes of the metal film thickness h and the metal loss factor η cause the shift of the resonant angle in the opposite direction to that of the dip angle and the shift of the resonant angle is smaller than that of the dip angle.

Extracting parameters from the angular reflection spectrum by the TCM method, we can obtain the total decay rate γ of the resonant mode, the external decay rate γ_e by radiation, the internal decay rate $\gamma_i = \gamma - \gamma_e$ caused by the metal loss, and the phase change ϕ caused by absorption in the direct reflection. Note that the decay rates are determined in accordance with the model of the TCM method. Because the far-field radiation from the resonant mode is restricted to a single port in the model of the TCM method, the external decay rate γ_e is determined only by the radiation to the zeroth-order diffraction. The decay caused by all other channels is expressed by the internal decay rate γ_i. The changes in these parameters are shown in Figs. 5(a) and 5(b). Figure 5(a) shows that the external decay rate γ_e and the total decay rate γ increase as the metal film thickness h decreases, while the internal decay rate γ_i decreases weakly. On the other hand, Fig. 5(b) shows that the internal decay rate γ_i and the total decay rate γ increase as the metal loss factor η increases, while the external decay rate γ_e decreases weakly. In both panels, the direct reflection phase ϕ changes in the same direction as that of the change in the internal decay rate γ_i.

The coincidence between the changes in the direct reflection phase ϕ and the internal decay rate γ_i is reasonable because both result from the absorption by the metal loss, whose effect decreases as the metal film thickness decreases. On the other hand, because the radiation from the resonance

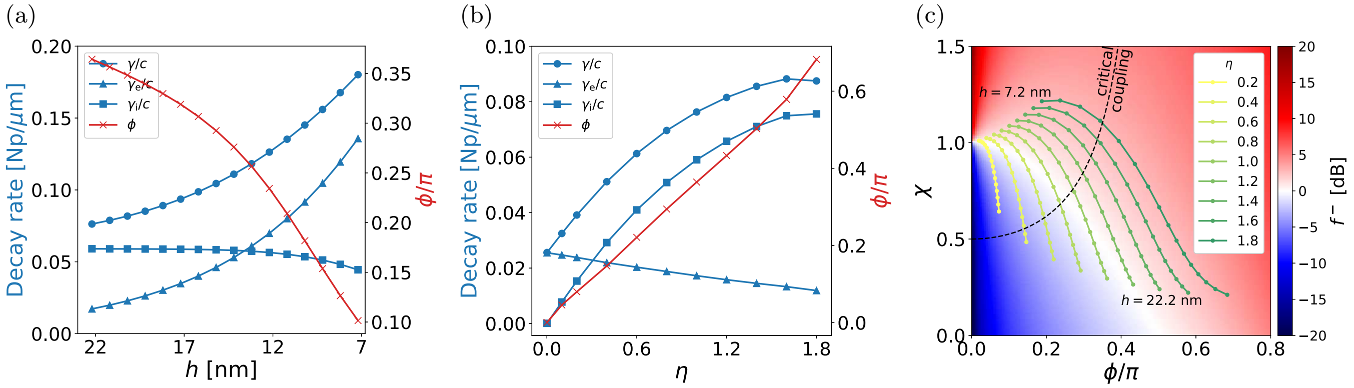

FIG. 5. Parameters extracted by the TCM method from the reflection spectrum of a flat metal film. (a), (b) Total decay rate γ, external decay rate γ_e, internal decay rate γ_i, and direct reflection phase ϕ as functions of (a) metal film thickness h and (b) metal loss factor η. (c) Relation between direct reflection phase ϕ and the ratio of decay rates χ depending on η and h plotted on a color map of spectral shape factor f^-, where h is varied from 22.2 nm (lower right) to 7.2 nm (upper left) by 1 nm.

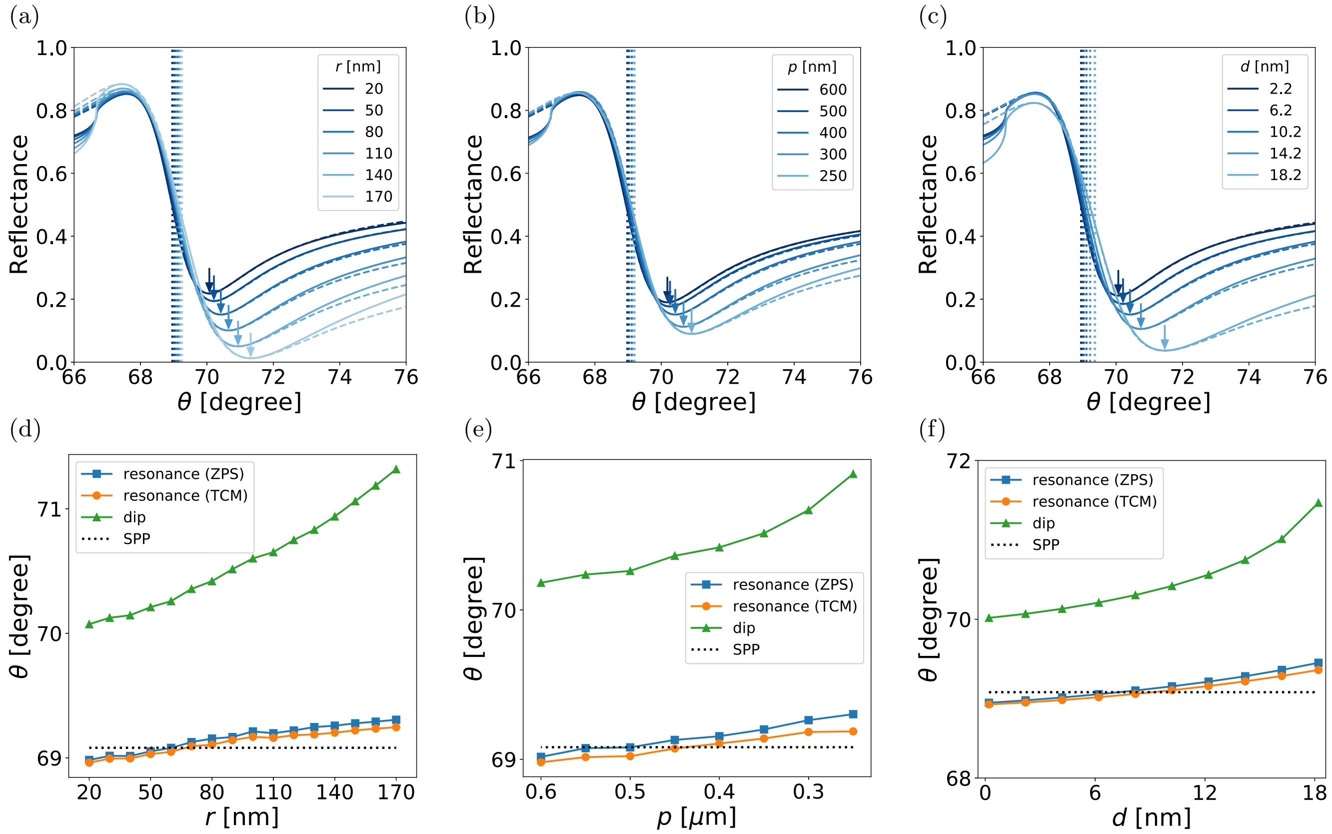

FIG. 6. Resonant and dip angles extracted for the nanodimple periodic array. (a)–(c) Dependence of the reflection spectrum on (a) dimple radius r, (b) period of dimple array p, and (c) depth of dimple d. Dotted lines depict the resonant angles extracted by the TCM method. Arrows denote the dip positions. (d)–(f) Resonant and dip angles as functions of (d) r, (e) p, and (f) d. Dotted line depicts the resonant angle obtained using the dispersion relation of SPP. Here, we assume that the thickness of the aluminum film outside the dimple is $h_0 = 22.2$ nm, and the fixed values of r, p, and d are 80, 400, and 10.2 nm, respectively.

caused by SPP at the NaCl solution side becomes stronger as the metal film thickness decreases, the external decay rate γ_e increases accordingly.

Figure 5(c) shows the changes in the direct reflection phase ϕ and the ratio of decay rates χ due to those in the metal thickness h and the metal loss factor η on the color map of SSF f^-. The lines with colors ranging from yellow to green denote the results for η from 0.2 to 1.8, as shown in the figure legend. The circles on the lines denote the parameter values for different values of h from 22.2 nm (lower right) to 7.2 nm (upper left). This figure indicates that the thickness of the metal film and the internal loss are reflected in the values of parameters χ and ϕ. In other words, h and η of a flat metal film can be deduced by determining the parameters χ and ϕ from the measured spectral shape of normalized reflectance.

D. Nanodimple periodic array

The inhomogeneity on the metal surface is expected to change the internal decay rate of SPP or the amplitude and phase of direct reflection. To estimate this change, we study the change in the reflection spectrum and the parameters due to the formation of a periodic array of cylindrical dimples on the surface of the aluminum film. In what follows, we assume that the thickness of the aluminum film outside the dimple is $h_0 = 22.2$ nm ($h + d = h_0$).

Figure 6 shows the dependencies of the reflection spectrum, dip angle, and resonant angle on the radius of the dimple cylinder r; period of the dimple array p; and depth of the dimple d. Figures 6(a) and 6(d) show the results in the case where the value of r is changed from 20 to 170 nm while fixing $d = 10.2$ nm and $p = 400$ nm. It is observed that as the dimple radius r increases, the dip angle [arrows in Fig. 6(a)] and resonant angle [dotted lines in Fig. 6(a)] shift to the wider-angle side. Note that the change in the dip angle is much larger than that in the resonant angle. Figures 6(b) and 6(e) show the results in the case where the value of p is changed from 600 to 250 nm while fixing $d = 10.2$ nm and $r = 80$ nm. It is observed that as the period p decreases, the dip angle and resonant angle shift to the wider-angle side. Moreover, the change in the dip angle is larger than that in the resonant angle. Figures 6(c) and 6(f) show the results in the case where the value of d is changed from 2.2 to 18.2 nm while fixing $r = 80$ nm and $p = 400$ nm. It is observed that as the depth d increases, the dip angle and resonant angle shift to the wider-angle side. Moreover, the change in the dip angle is larger than that in the resonant angle.

Figure 7 shows the decay rates γ, γ_e, and γ_i and the direct reflection phase ϕ extracted by the TCM method. Figures 7(a), 7(b), and 7(c) show the results for the same condition as that in Figs. 6(a), 6(b), and 6(c), respectively. These results indicate that an increase in the dimple radius

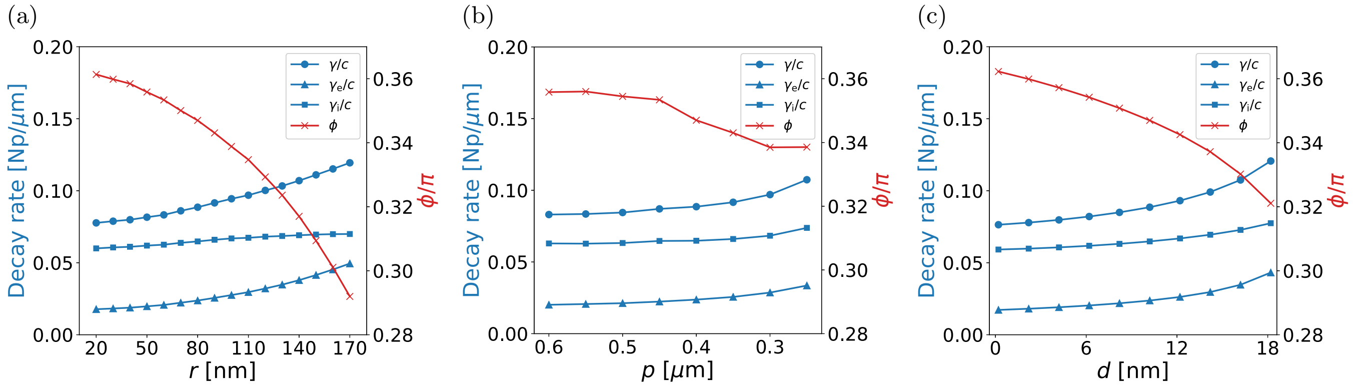

FIG. 7. Parameters extracted by the TCM method from the reflection spectrum of the nanodimple periodic array. Total decay rate γ, external decay rate γ_e, internal decay rate γ_i, and direct reflection phase ϕ as functions of (a) dimple radius r, (b) period of dimple array p, and (c) depth of dimple d. The system configuration condition is the same as that in Fig. 6.

r, decrease in the period of dimple array p, or increase in the depth of dimple d, namely, increase in the ratio of the region of dimple in the metal film region, results in an increase in the decay rate and decrease in ϕ. However, the increase in the internal decay rate γ_i is rather small, and that in the decay rate mainly originates from the increase in the external decay rate γ_e. This tendency is similar to that observed when the thickness of a flat metal film is decreased. It can be interpreted that the formation of dimples reduces the "effective thickness" of the metal film and enhances the radiation from SPP at the NaCl solution side to the substrate side, to increase the external decay rate. Hereafter, we use the term "effective thickness" of the metal film for the thickness of a flat metal film without a dimple that gives the same external decay rate as the metal film with dimples. Note that the electromagnetic field inside the metal region decays exponentially, which results in the exponential dependence of the external decay rate on the metal film thickness. Therefore, the most remarkable effect of the reduction of the metal film thickness appears in the enhancement of external decay. The change in the direct reflection phase ϕ can also be explained by the decrease in the effective thickness of the metal film, but it can also be interpreted as a result of effective decrease of the metal loss factor η.

The trend of the internal decay rate γ_i is opposite to that in the case of change in the thickness of a flat metal film. This behavior indicates that the diffraction of SPP by the dimple array enhances the internal decay. However, the change in the direct reflection phase ϕ is mainly determined by the material loss (volume of metal region) because the diffraction produced by the periodic array with the period comparable to the wavelength is restricted to a few diffraction orders and the influence on the direct reflection process is weak.

E. Random array

For the periodic array discussed in the previous section, the effect of diffusive scattering is weak because the radiative diffraction order is restricted. In this section, we discuss a system with randomly distributed dimples in order to include the effect of diffusive scattering. Figure 8 shows the dependence of (a) the angular spectrum, (b) dip and resonant angles, and (c) decay rates and the direct reflection phase on the depth of dimple d for a sample whose extracted values are near the

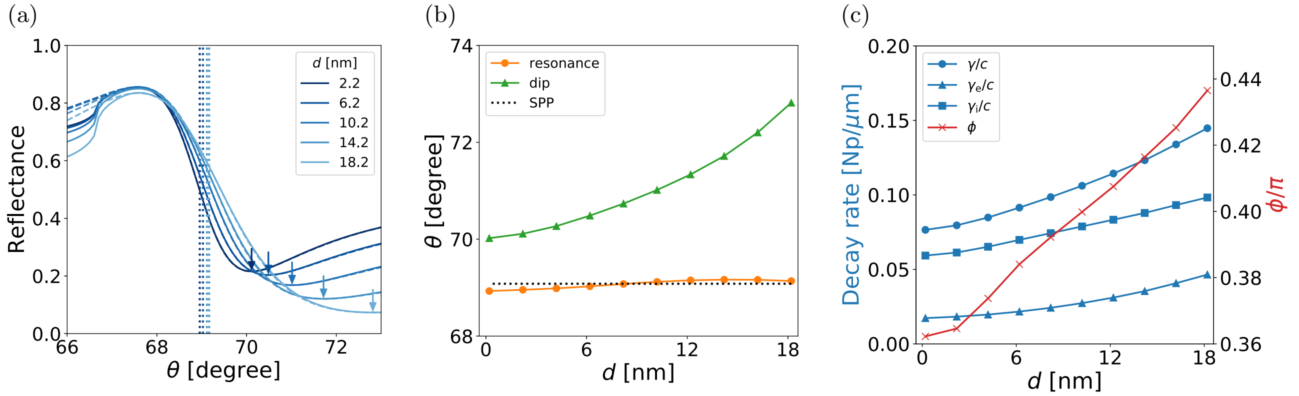

FIG. 8. Parameters extracted by the TCM method from the reflection spectrum of the nanodimple random array. (a) Dependence of the reflection spectrum on the depth of dimple d. Dotted lines depict the resonant angles. Arrows denote the dip positions. (b) Resonant angle and dip angle as functions of d. Dotted line depicts the resonant angle obtained using the dispersion relation of SPP. (c) Total decay rate γ, external decay rate γ_e, internal decay rate γ_i, and direct reflection phase ϕ as functions of d. Here, we assume that the thickness of the aluminum film outside the dimple is $h_0 = 22.2$ nm, and the radius of the dimple is set to 80 nm.

averaged values of randomly produced 100 samples. Here, the dimple radius r is set to 80 nm, and the depth of dimple d is changed from 0.2 to 18.2 nm for the same distribution of dimples in the xy plane. In addition, in this section, the thickness of the aluminum film outside the dimple is assumed to be $h_0 = 22.2$ nm.

Comparing the results for the periodic array in Figs. 6(c) and 6(f) and those for the random array in Figs. 8(a) and 8(b), it is found that the extension of the width of the dip and the shift of the dip angle due to an increase in the depth of dimple d are larger in the random array. In addition, Figs. 7(c) and 8(c) show that the direct reflection phase ϕ increases with d in a random array, contrary to the case of periodic array. These results are similar to those obtained when the metal loss factor η is increased in a flat metal film. Thus, the introduction of a random dimple array produces a similar effect as that of an increase in metal loss. The diffusive scattering produced by the random array suppresses the direct specular reflection, like absorption.

F. Effect of dimple array on parameters

From the above consideration, it is deduced that one of the effects of dimple formation is the reduction in the effective thickness of the aluminum film. This results in an increase in external decay, namely, the enhancement of radiation from the resonant mode. The radiation from the resonant mode is limited by the tunneling process within the metal region, which depends exponentially on the product of the decay rate of the evanescent field in the z direction, $\gamma_z = \sqrt{k_{\mathrm{SPP}}^2 - \mathrm{Re}[\varepsilon_{\mathrm{Al}}]\omega_{\mathrm{i}}^2/c^2}$, and the thickness of the metal region. Here, k_{SPP} is the wave number of SPP at an angular frequency of ω_{i}. Therefore, we define the effective thickness of the metal film as follows:

$$\exp(-2\gamma_z h_{\mathrm{eff}}) = \frac{\pi r^2}{p^2}\exp(-2\gamma_z h) + \left(1 - \frac{\pi r^2}{p^2}\right)\exp(-2\gamma_z h_0), \qquad (16)$$

where $h_0 = 22.2$ nm and h denote the thickness of the aluminum film outside the dimple and that left below the bottom of the dimple, respectively. The period of array p is taken to be 400 nm in the random array case, considering the average density of the dimples.

Figure 9 shows the relation between the value of effective film thickness h_{eff} defined by Eq. (16) and the external decay rate. The black solid line depicts the results for a flat aluminum film with thickness h_{eff}. The light-blue dashed line denotes exponential dependence on h_{eff}, expressed by the left-hand side of Eq. (16), based on the value at $h_{\mathrm{eff}} = 22.2$ nm. All data coincide well, which shows the validity of the estimation of effective thickness using Eq. (16). Thus, we can evaluate h_{eff} from the value of the external decay rate γ_{e} assuming the exponential dependence between them, and use it as an index for corrosion.

In Fig. 10(a), the values of the ratio of decay rates χ and the direct reflection phase ϕ extracted from the reflection spectra for various conditions of the periodic array (yellow circles) and random array (green squares) of dimples are plotted on the color map of the spectral shape factor (SSF) f^-, as in Fig. 5(c). The black solid line depicts the result of a flat aluminum film with various thicknesses decreasing from the lower right to upper left, where the metal loss factor η is fixed

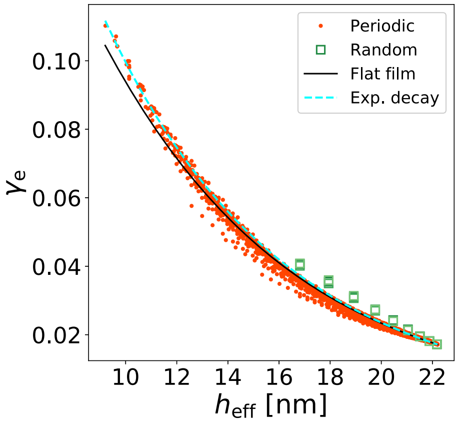

FIG. 9. Relation between the external decay rate γ_{e} and the effective aluminum thickness h_{eff} for nanodimple periodic array (red dots), nanodimple random array (green squares), and flat aluminum film (black solid line). The light-blue dashed line depicts the exponential dependence on h_{eff} based on the value at $h_{\mathrm{eff}} = 22.2$ nm.

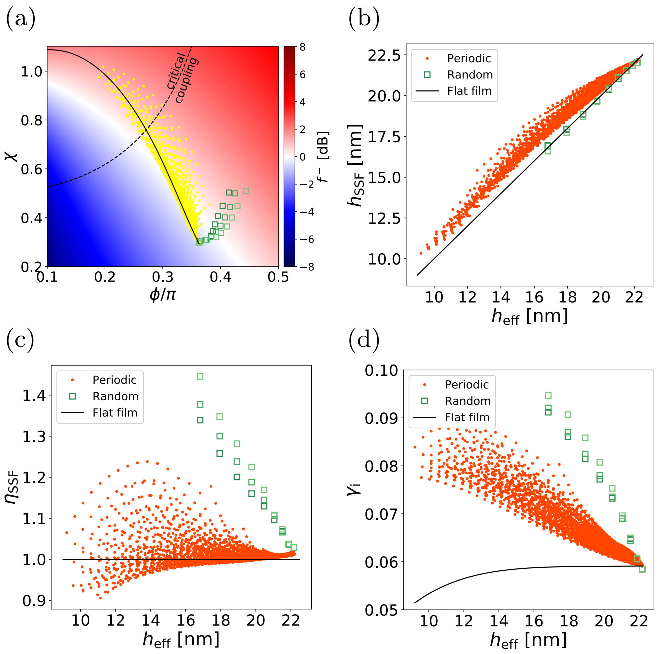

FIG. 10. Parameters extracted by the TCM method from the reflection spectra for various configurations of nanodimples. (a) Direct reflection phase ϕ and ratio of decay rates χ for periodic array (yellow circles) and random array (green squares) plotted on the color map of the spectral shape factor f^-. (b), (c) Thickness h_{SSF} and the metal loss factor η_{SSF} for the flat metal film that gives the same shape of the normalized reflection spectrum as the dimple array system with the effective thickness h_{eff}. (d) Internal decay rate γ_{i} as a function of h_{eff}. Red dots, green squares, and the black solid line denote the results for nanodimple periodic array, nanodimple random array, and flat aluminum film, respectively.

to 1. Using the results shown in Fig. 5(c), we can deduce the thickness of the aluminum film $h_{\rm SSF}$ and the metal loss factor $\eta_{\rm SSF}$ for the metal film that provides the values of χ, ϕ, and f^- at the points in Fig. 10(a). Thus, we obtain a flat metal film model with thickness $h_{\rm SSF}$ and metal loss factor $\eta_{\rm SSF}$ for each dimple array system. This model gives the same shape of the normalized reflection spectrum as the dimple array system. Figures 10(b) and 10(c) show $h_{\rm SSF}$ and $\eta_{\rm SSF}$ as functions of effective thickness $h_{\rm eff}$ for periodic arrays (red dots), random arrays (green squares), and a flat aluminum film (black solid line). Figure 10(b) shows that $h_{\rm SSF}$ corresponds rather well with $h_{\rm eff}$, which is consistent with the notion that one of the effects of the dimple array is to reduce the effective thickness of the aluminum film and result in the exponential enhancement of radiative decay. While from Fig. 10(c), another effect of the dimple array can be considered to alter (enhance in most cases) the imaginary part of the permittivity of aluminum effectively. This effect seems to be produced by diffusive scattering, which depends on the configuration of the dimples. Indeed, we can see that random arrays provide higher enhancement than the periodic array.

These effects of the dimple array appear in each parameter value, such as the internal decay rate $\gamma_{\rm i}$ shown in Fig. 10(d) and the direct reflection coefficient $r_{\rm d}$ shown in Fig. S1 in Supplemental Material [30]. These parameters strongly depend on the structure and distribution of dimples, even though they provide the same effective thickness. Especially, the plots of $\gamma_{\rm i}$ for the flat films, periodic arrays, and random arrays are distributed separately. Note that we studied only 100 samples of random distribution of dimples, in which the variation of distribution is quite limited and rare cases, such as quasiperiodic distributions, are not included. These results indicate that a more detailed characterization of the metal surface condition can be achieved by analyzing these parameters systematically, e.g., by using machine learning with much bigger data sets. However, this will be taken up in the future.

Finally, we comment about the effect of system geometry on the parameters. Otto configuration is another setup used in the ATR method, in which a thick metal film is positioned close to a prism [39]. It has been shown that the Fano resonance occurs also in the Otto configuration in [8]. Therefore, the Otto configuration may also be used to detect pitting corrosion. We summarize the results of corresponding calculation for the Otto configuration in the Supplemental Material [30]. As shown in Fig. S7, the shift of the dip angle due to the growth of dimples is as small as the shift of the resonant angle. Therefore, the Kretschmann configuration is superior for the detection of pitting corrosion on nanoscale. Note that Fig. S7 shows that the shift of the resonant angle calculated using the SCM method for the both configuration is comparable to the result of the perturbation theory [40,41] for the SPP resonance on the aluminum surface with the same random array of nanodimples, and it is much smaller than the shift of dip angle in the Kretschmann configuration. In a real pitting corrosion, various shapes of dimples may be created. The geometry of dimple may affect the ATR spectrum. Because the effective thickness defined by Eq. (16) is determined only by the area $A = \pi r^2$ and the thickness h of the metal film left below the dimple array, we expect that the estimation of the effective thickness using Eq. (16) is applicable to the case of other geometry, such as spherical dimple, by introducing some geometrical correction to the area A and the thickness h. Experimental or numerical confirmation of this expectation is necessary, but it will also be taken up in the future.

IV. CONCLUSIONS

In this paper, we have shown the possibility of evaluating the surface roughness of a metal film by analyzing the ATR spectrum from the viewpoint of Fano resonance. Using the temporal coupled-mode method, it was found that the geometrical feature of the ATR spectrum is characterized by a single shape factor, which is determined by the following two parameters: Direct reflection phase and ratio of decay rates. Based on this information, we have developed a method to extract key parameters, such as internal and external decay rates, from spectral data, and shown that these parameters provide corrosion information such as the effective thickness of the metal film and the distribution of nanosized dimples. These results form the basis for developing a method for characterizing the initial stage of pitting corrosion on a metal surface using plasmonic ATR.

ACKNOWLEDGMENTS

This study was supported by JSPS KAKENHI Grants No. JP18K04980 and No. JP18K04979.

[1] B. Liedberg, C. Nylander, and I. Lunström, Sens. Actuators **4**, 299 (1983).

[2] J. Homola, S. S. Yee, and G. Gauglitz, Sens. Actuators B **54**, 3 (1999).

[3] J. Homola, Chem. Rev. **108**, 462 (2008).

[4] E. Kretschmann and H. Raether, Z. Naturforsch. A **23**, 2135 (1968).

[5] E. Kretschmann, Z. Phys. A **241**, 313 (1971).

[6] H. Raether, *Surface Plasmons on Smooth and Rough Surfaces and on Gratings* (Springer, Berlin, 1988).

[7] A. P. Vinogradov, A. V. Dorofeenko, A. A. Pukhov, and A. A. Lisyansky, Phys. Rev. B **97**, 235407 (2018).

[8] D. V. Nesterenko, S. Hayashi, and Z. Sekkat, Phys. Rev. B **97**, 235437 (2018).

[9] U. Fano, Phys. Rev. **124**, 1866 (1961).

[10] A. Braundmeier and E. Arakawa, J. Phys. Chem. Solids **35**, 517 (1974).

[11] D. Hornauer, H. Kapitza, and H. Raether, J. Phys. D: Appl. Phys. **7**, L100 (1974).

[12] R. Orlowski, P. Urner, and D.-L. Hornauer, Surf. Sci. **82**, 69 (1979).

[13] S. O. Sari, D. K. Cohen, and K. D. Scherkoske, Phys. Rev. B **21**, 2162 (1980).

[14] X. Chen, M. Pan, and K. Jiang, Microelectron. Eng. **87**, 790

(2010), the 35th International Conference on Micro- and Nano-Engineering (MNE).

[15] S. Agarwal, Y. Prajapati, and V. Singh, Opt. Commun. **383**, 113 (2017).

[16] R. J. Bussjager and H. A. Macleod, Appl. Opt. **35**, 5044 (1996).

[17] L. C. Oliveira, A. Herbster, C. da Silva Moreira, F. H. Neff, and A. M. N. Lima, IEEE Sens. J. **17**, 6258 (2017).

[18] H. Raether, Surf. Sci. **125**, 624 (1983).

[19] E. Fontana and R. H. Pantell, Phys. Rev. B **37**, 3164 (1988).

[20] G. S. Frankel, J. Electrochem. Soc. **145**, 2186 (1998).

[21] H. Kaesche, Pitting corrosion, in *Corrosion of Metals: Physicochemical Principles and Current Problems* (Springer, Berlin, 2003), pp. 324–388.

[22] E. McCafferty, *Introduction to Corrosion Science* (Springer, New York, 2010).

[23] H. A. Haus, *Waves and Fields in Optoelectronics* (Prentice Hall, Englewood Cliffs, NJ, 1983).

[24] S. Fan, W. Suh, and J. D. Joannopoulos, J. Opt. Soc. Am. A **20**, 569 (2003).

[25] M. Nishida and Y. Kadoya, in *Fano Resonances in Optics and Microwaves*, edited by E. Kamenetskii, A. Sadreev, and A. Miroshnichenko (Springer, Berlin, 2018), Chap. 14, pp. 331–355.

[26] F. J. García-Vidal, E. Moreno, J. A. Porto, and L. Martín-Moreno, Phys. Rev. Lett. **95**, 103901 (2005).

[27] M. Nishida, N. Hatakenaka, and Y. Kadoya, Phys. Rev. B **91**, 235406 (2015).

[28] A. D. Rakić, A. B. Djurišić, J. M. Elazar, and M. L. Majewski, Appl. Opt. **37**, 5271 (1998).

[29] J. D. Joannopoulos, S. G. Johnson, J. N. Winn, and R. D. Meade, *Photonic Crystals: Molding the Flow of Light*, 2nd ed. (Princeton University Press, Princeton, NJ, 2008).

[30] See Supplemental Material at http://link.aps.org/supplemental/10.1103/PhysRevB.101.085414 for the derivations of the TCM and the SCM methods, the results for the Otto configuration, and the comparison with the results obtained by a perturbative treatment.

[31] F. de León-Pérez, G. Brucoli, F. J. García-Vidal, and L. Martín-Moreno, New J. Phys. **10**, 105017 (2008).

[32] A. Roberts, J. Opt. Soc. Am. A **4**, 1970 (1987).

[33] H. A. Lorentz, Versl. Kon. Akad. Wetensch. Amsterdam **4**, 176 (1896).

[34] A. T. de Hoop, Appl. Sci. Res., Sect. B **8**, 135 (1960).

[35] P. Lalanne, J. P. Hugonin, and J. C. Rodier, Phys. Rev. Lett. **95**, 263902 (2005).

[36] R. J. Potton, Rep. Prog. Phys. **67**, 717 (2004).

[37] G. Eriksson, *2007 IEEE International Symposium on Electromagnetic Compatibility* (IEEE, Piscataway, NJ, 2007), pp. 1–6.

[38] T. Weiss, Advanced numerical and semi-analytical scattering matrix calculations for modern nano-optics, Ph.D. thesis, University of Stuttgart, 2011.

[39] A. Otto, Z. Phys. A **216**, 398 (1968).

[40] E. Kröger and E. Kretschmann, Phys. Status Solidi B **76**, 515 (1976).

[41] F. Toigo, A. Marvin, V. Celli, and N. R. Hill, Phys. Rev. B **15**, 5618 (1977).